A NUMERICAL SIMULATION OF SINGLE AND TWO-PHASE FLOW IN POROUS MEDIA; A PORE-SCALE OBSERVATION OF EFFECTIVE MICROSCOPIC FORCES

M. Aboukhedr*, K. Vogiatzaki, N. Mitroglou, M. Gavaises
Department of Mechanical Engineering,
International Institute for Cavitation Research (ICR)
City University London
UK

KEYWORDS
Pore-scale modelling, openFOAM, Hydraulic conductivity, Navier-Stokes equations, Volume of Fluid.

1. ABSTRACT

Modelling fluid flow in rock porous media is a challenging physical problem. Simplified macroscopic flow models, such as the well-known Darcy's law, fail to predict accurately the pressure drop because many flow parameters are not considered while simplifications are made for the multi-scale structure of the rocks. In order to improve the physical understanding for such flows and the accuracy of existent models, there is a need for realistic geometries to be investigated. The present work describes initially single-phase flow simulations performed on numerical grids obtained from reconstruction of 2D images of rock porous media found in the open literature using ANSA®. The results in terms of preferential paths and tortuosity are compared with experiments. Following, multiphase flow models have been utilised focusing on the capturing of the liquid-gas interface motion. It is concluded that for such complex porous rock problems, the multi-scale flow development is grid dependent.

2. INTRODUCTION

Characterisation of single and multi-phase flow through porous media is of paramount importance in many applications such as hydrocarbon recovery, CO2 storage in underground reservoirs, ion transfer through membranes and drag delivery in biological tissues to name a few. One of the challenges when porous media are investigated numerically is their multi-scale nature. Just to give an example, in applications involving oil extractions, the scales that ideally should be accounted for in a simulation range from kilometers (well size) to micrometers (rock pore throat size). With the current numerical capabilities an "all scale" analysis is not feasible. Instead the efforts up to date focus on (a) performing simulations at the micro scale (1–4) and (b) establishing upscaling relationships (5)(6–8). One of the most well know upscaling laws is Darcy's law (9) that provides a linear relationship between the instantaneous discharge rate through a porous medium, the viscosity of the fluid and the pressure drop over a given distance. Although it was initially introduced as a phenomenologicaly derived equation, it can be proved that integration of the flow equations at the Stokes regime at the micro-scale can result to Darcy's Law at the macro-scale (10).

The accuracy of the existent upscaling techniques depend on the fundamental understanding of the physical characteristics of the solid and the fluids that occupy the pore space. These include the capillary pressure, relative permeability and hydraulic conductivity. Equally important is the numerical representation of the actual geometry under investigation involving proper selection of boundary conditions, since only a small part of the real material is investigated, numerical algorithms to capture interphases between fluids and of course grid quality. Until the 1990s, attempts to relate physical properties of a rock to its microstructure were mainly limited by the difficulty of adequately describe experimentally the complex nature of the pore space. Direct measurements of a 3D microstructure are now available via X-ray computed microtomography (11–14). In practice though, information about the microstructure of porous materials is still often limited to 2D thin section images.

A number of approaches has been suggested in the literature in order to reconstruct 3D porous media from 2D thin section images. Early efforts are known as statistical models and are based on matching the statistical properties, such as porosity, correlation and lineal path functions of 2D thin section images to 3D models (15,16). Another group of models are known as process-based models and try to account for the fact that the pore structure is often the result of physical process (17,18). Although a detailed review of all the existent reconstruction models is out of the context of this paper, it should be noted that the common drawback of all these attempts is that reconstructions may differ significantly from the original sample in their geometric connectivity as well as the geometric characteristics of the actual grains (such as sharp corners representation) that are in reality very important for the accurate pore scale computations.

In the current work we present a simple image reconstruction technique from pictures in literature, maintaining the porosity and permeability of the original scanned sample. Reconstruction is performed on a "realistic" sample using photographs from the literature and maintains the grain characteristics (size geometrical features etc) of the real sample. The pore-scale geometry has been reconstructed and refined using ANSA® pre-processing tools that allow for full-model build up, from image to ready-to-run solver input file (19). The structure of the paper is the following: in Section 3 we present the properties of the Brea stone sample used (20,21) as well as the reconstruction technique. The image analysis algorithms are presented and the impact of image segmentation procedure on calculation of porosity is assessed. Following the reconstruction section, is section 4, we present some indicative calculations of single and multiphase flows through the 2D reconstructed samples in order to assess the effect of the grid quality and resolution on the flow field results.

3. IMAGE BASED MESH GENERATION

i. EXPERIMENTAL SAMPLE

In the current paper we based our reconstruction process on one slice, obtained from 2D images of Berea sandstone (20) that is shown in Fig. (1-a). Berea sandstone has been used by the petroleum industry for many years as a standard material in core analysis mostly because the rock is relatively homogenous and well characterized. It is made up of well-sorted predominately quartz grains, but it also contains minor amounts of feldspar, dolomite, and clays (22,23). The sandstone used in the study was a porous media of 575×488×5 μm in size with a mean grain diameter of 50 μm. The thin slice of Berea sandstone was imaged through an optical microscope and then digitized by Hornbrook et al. (20,24).

ii. 2D IMAGE RECONSTRUCTION

Segmentation process is used to identify -within the matrix/image- what pixels belong to each object of interest. Thresholding allows for an object to be identified by specifying minimum and maximum values of signal strength. Other algorithms such as Floodfill and Level Set Methods (25,26) can also be used for automated or semi-automated segmentation. In some cases with poor quality images/scans, less automated techniques such as the manual segmentation can be used. Bitmap tool (27–29) was used for converting grayscale binary images -shown in Fig. (1-b)- to mapped image (lines) in Fig. (1-c). The resulting file of the mapping process (.stl), was then sent to ANSA for vector clean up and geometry editing. The curve modifier in ANSA (i.e modify and Cons2Curv) was used to reattach the missing parts and then to smooth the sharp edges for numerical reconstruction. Following, the general topology was checked with 'Topo' tool, and the void volume was sealed by air space; the solid grain particles were excluded.

iii. MESH GENERATION

After reconstructing the 2D geometries, we proceed with the meshing process. The segmented topological model is simultaneously meshed based on an orthotropic grid intersected by interfaces defining the boundaries. The Cartesian mesh of the whole volume is defined to consist of orthogonal tetrahedralised or of perfect quads at boundary interfaces based on cutting planes defined by interpolation points. Smooth boundaries are obtained by adjusting the interpolation points using a smoothing tool [Shell Mesh reshape and reconstruct]. The process of mapping after smoothing results in either a mixed tetrahedral/hexahedral mesh or in a pure tetrahedral mesh and incorporates an

adaptive meshing scheme supported by the CFD code used in this work (openFOAM). The adaptive meshing scheme preserves the topology but reduces the mesh density where possible towards the interior of the mesh by agglomerating small-size hexahedra into larger ones and generating transitional small tetrahedral. The approach is fully automated and robust, creating smooth meshes with low element distortions regardless of the complexity of the segmented data.

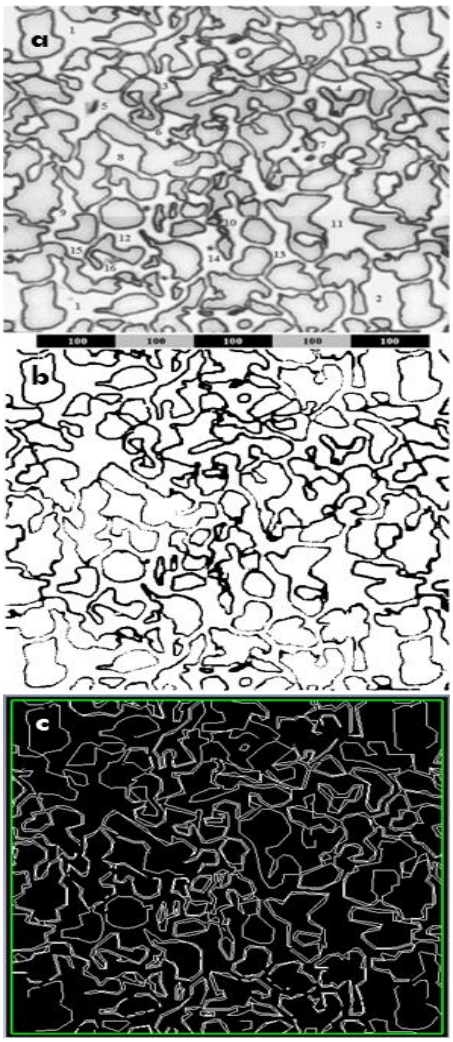

Figure 1: Illustration of 2D porous media reconstruction (a) Image of Berea sandstone by Hornbrook et al. (20,24), (b) Grayscale segmentation result using MATLAB, (c) Bitmap segmentation used to convert grey scale to vector image before cleaning up.

The approach adopted allows for an arbitrary number of different volumes to be meshed. As neighbouring sub-domains share a common cutting surface, this ensures a node to node correspondence at the boundaries between different meshed volumes, thus trivially satisfying the geometrical constraints at the boundary. In order to complete the reconstruction process, we need to ensure that the model created represents the 2D images in terms of main geometric characteristics and that it does not add/reduce artificially the porosity. The model porosity was calculated in ANSA by measuring the domain volume and comparing it to the experimental values. Although different grid sizes may result in slightly different porosity values, the porosity of the micromodel used here has been experimentally determined to be 37% and computationally to be 40%.

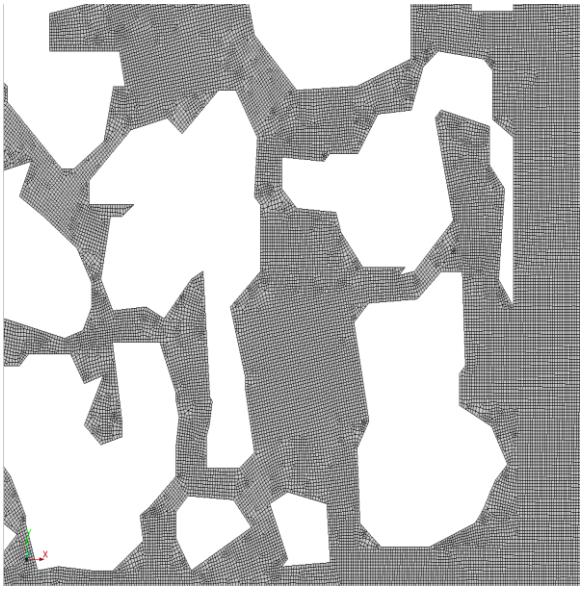

Figure 2: Grid around a sharp edged grain

Volume evaluation was made with the statistical tools available in ANSA; these assist the mesh generation quality to match the acceptable openFOAM mesh parameters. The elements' skewness analysis tends to have low skewed elements at almost 98% mesh points after mesh refinement (which will lead to good convergence during the calculation). Due to the extreme refinement in sharp areas, the number of cells increases and as a direct consequence the computational time will increase. The same test had been carried out for the elements aspect ratio. In this test, we found that about 60% of the elements is relatively high, which may cause some problems in convergence. For accurate and stable simulation performance, "non orthogonality" and "minimum length quality" test had been made to assure the mesh quality is fulfilling openFOAM criteria (orthogonality should be less than 60-70 degree). The test had been controlled using ANSA CFD mesh tool and the results are shown in Table (1). The last step was the scaling of the model and exporting to openFOAM 2.3x files; these is shown in Fig. (2).

Solid Non Orthogonality Quality NON ORTHOGONALITY [OPENFOAM]

Solid Non Orthogonality Table						
ID of Element with min value				MIN Value		
19932737				0		
ID of Element with max value				MAX Value		
21865314				62.7082		
Class					No of Elements	Perc(%)
1	From:	-∞	To:	0	0	0
2	From:	0	To:	20	10404011	59.9253
3	From:	20	To:	40	6726329	38.7425
4	From:	40	To:	60	231294	1.33221
5	From:	60	To:	70	2	1.15197e-05
6	From:	70	To:	90	0	0
7	From:	90	To:	+∞	0	0
Out of any class limit					0	0
TOTAL					17361636	

Solid Non Orthogonality Graph

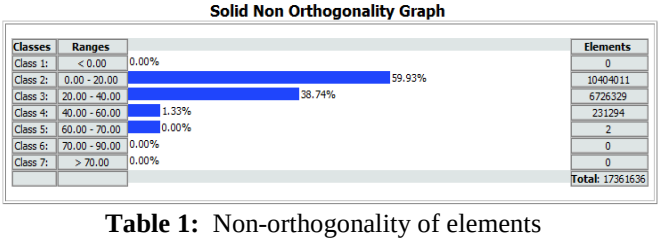

Table 1: Non-orthogonality of elements

4. SIMULATION SPECIFICS

For the current work OpenFOAM was used, which is a free, open source CFD software package developed by OpenCFD Ltd (31). Both single-phase (water injection through a 2D geometry Fig (4)) and two-phase flow (oil drainage by water injection Fig (6)) simulations have been performed. The aim was to investigate how the image reconstruction technique and the grid quality affects predictions of flow through the specific porous media. For the single-phase simulations, the standard laminar Navier-Stokes equations of mass and momentum conservation. For multiphase flows the standard Volume of Fluid algorithm (VOF) (32) is used. This method tracks the interface between the two fluids while an additional term accounting for surface tension forces between the two liquids was added to the momentum equation. The fluids for both single and multiphase runs are considered incompressible and invincible. The flow is isothermal. The physical properties of water and oil as well as the inlet conditions are summarised in the following Table (2).

Parameter	Symbol (units)	Value
Volumetric flow rate (single phase)	Q (m^3/s)	8.333e-11
Volumetric flow rate (two-phase)	Q (m^3/s)	1e-10
Fluid density (water)	ρ (kg/m^3)	998
Fluid dynamic viscosity (water)	μ ($\frac{Ns}{m^2}$)	8.88e-4
Fluid density (oil)	ρ (kg/m^3)	835
Fluid dynamic viscosity (oil)	μ ($\frac{Ns}{m^2}$)	0.1
Surface tension (water to oil)	N/m	0.048
Contact angle at the triple line	degrees	45

Table 2: Fluid properties and initial conditions

For the two-phase flow calculations in cells that the two phases coexist density and viscosity are calculated as the volume arithmetic mean of the two components. Regarding the inlet conditions it should be noted that: a) The mass flow rate for the single flow was determined in order to match the experimental conditions presented in (21). b) The mass flow rate for the multiphase flow is considerably higher. Experiments were not available for the Barea stone for multiphase calculations and thus a relatively high mass flow rate was chosen (although still the capillary number remains low [1e-4]) for better numerical stability and in order to avoid the effect of spurious velocities.

The diffusive fluxes are approximated using a second order central difference scheme. The convection terms are discretized using a second-order central difference scheme. The PISO algorithm for collocated variables arrangement is used to solve the pressure equation. The linear equation system is solved implicitly by the vectorized incomplete PBICG method for velocity. The pressure and velocity fields on a non-staggered grid are coupled by the momentum interpolation technique PCG. Moreover, since the length-scales involved in this investigation of the flow in the pores of the media are very small (at the order of hundreds of micrometres and less), the Knudsen number (Ku) was checked and it was confirmed that the continuum hypothesis for the fluids holds. Non non-permeable and no-slip boundary conditions were applied on the walls. The model boundary conditions can be seen in Fig. (3). Each of the simulations for the single-phase flow were performed on a grid of ten million cells and the running time was proximately 24 hours. For the multiphase flow simulations only a section of the single phase geometry was used in order to save computational time. The presence of the interphase and the use of VOF in order to track it would require a very low Currant number to succeed stability which slows down the calculations. The simulation was preformed on a base grid of two million cells (maintaining the same cell size as for the single phase geometry) and running time was about 80 hours on 24 cores. The grid resolution was further enhanced in areas of interest (such as two-liquids interphase) with the use of adaptive grid refinement described in the previous section.

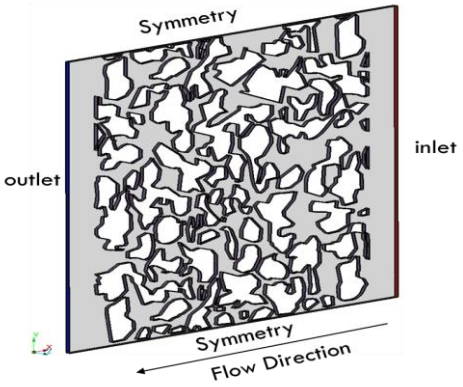

Figure 3: Schematic of the boundary conditions.

5. RESULTS

In this section indicative results from single and multiphase flow calculations are presented. The single-phase calculations where performed in conditions relevant to water injection when shale rock fracturing is considered. In this application water with solid grains (sand) is injected. The water allows for the existent (tight) natural fracks to widen and then the sand is deposited in the pore throat to maintain the voids open. Through this process what is of interest is to know the preferential paths of the flow. Preferential flow refers to the uneven and often rapid movement of water and solutes through porous media. The preferential flow will define the paths that the sand grain will follow. In the section entitled 'Single Flow' we present results of the 2D model for two quantities that link closely to the preferential paths e.g. hydraulic conductivity and tortuosity. In the section entitled 'Multiphase Flow' oil drainage by water injection was the simulation target. Water injection, also known as water-flood, is a form of this secondary Enhanced Oil Recovery (EOR) production process (33).

a. Single Flow

i. HYDRAULIC CONDUCTIVITY

Hydraulic conductivity is a measure of a material's capacity to transmit a fluid. It depends both on material properties (intrinsic permeability) and fluid properties (the degree of saturation, the density and viscosity). It is defined as a constant of proportionality relating the specific discharge of a porous medium under a unit hydraulic

gradient in Darcy's law. In the current study the hydraulic conductivity was numerically calculated as:

$$k_{num} = \frac{\frac{\varepsilon}{A_{pore}} \cdot \int_{A_{pore}} vdA}{\frac{\nabla p}{\rho g}/L} \quad (1)$$

with A the cross sectional area [m^2], p the pressure difference [Pa] and L [m] the sample length. Following the calculated hydraulic conductivities were converted to rock permeability based on Eq. (2) and results were compared with experimental values. Two different grids (differing one order of magnitude) were used. As it can be seen in Table (3) the calculated permeability even for the 10M cells grid diverges one order of magnitude from the experimental value. The results are highly grid dependent as by changing the grid size one order of magnitude (from 1M to 10 M) the accuracy of the predictions change one order of magnitude as well.

$$k_{per} = K_{hyd} \frac{\mu}{\rho g} \quad (2)$$

Model	Average permeability m^2
Experimental	1e-11 m^2
Numerical 10M (Fine grid)	1.024e-12 m^2
Numerical 1M (Coarse grid)	6.7e-13 m^2

Table 3: Comparison between different permeabilities

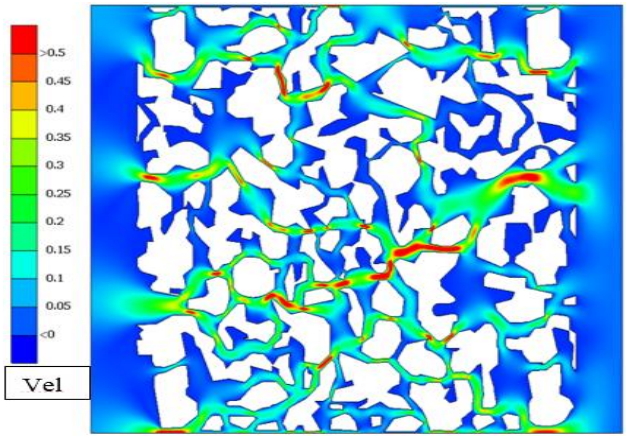

Figure 4: Velocity distribution in m/s.

In Figure (4) we show the water velocity distribution through the simulated slice. It can be seen that the flow accelerates not only through the small pores as expected due to natural higher pressure drop, but also through wider throats and this is a phenomenon associated with the surrounding material structure. Areas with higher velocities can be considered as indicators of the preferential path of a massless particle introduced in the flow

ii. ***TORTUOCITY EFFECTS***

In transport through porous media the fluid follows a tortuous path around the grains, which impacts the diffusion and the advection of the fluid and contaminants. The tortuosity of a porous media can be defined in terms of the porous sample under consideration L and the length of the actual path that the a massless particle introduced in the flow will follow (length $\boldsymbol{\lambda}$) as $\boldsymbol{T = \frac{\lambda}{L} \geq 1}$. For the numerical calculation of tortuosity we use a summation over selected number N of stream lines associated with the preferential paths of the flow (35):

$$T = \frac{1}{L}\frac{1}{N}\sum_{j=1}^{N} \lambda(x) \quad (3)\ \text{I}$$

In Figure (5) we show a zoom in of the flow around a grain of Fig. (4). The picture on the right shows the path that a very small particle (considered almost massless) will follow and is taken from the experiments conducted by Sirivithayapakorn el. al. (21). The black line -indicating the particle trajectory- follows the general flow direction (from inlet to outlet) up to point that meets an obstacle. There the flow actually diverges around the grain. The particle will follow the direction of the "preferential path", or in other words the path that the flow accelerates more. For the specific grain particles will move preferentially through the upper part of the grain. The snapshot on the left shows the streamline of the flow. The brighter the colour, the smaller the velocity of the individual streamline. As it can be seen, the numerical results of the streamlines with higher velocities coincide with the experimental results from the particle trajectory. It should be noted that in the experiment a number of particles was used in order to demonstrate that there is actually a preferential path rather than a random walk of these particles. From these plots of the streamlines the effective length of each traveling particle can be calculated and the tortuosity can then be evaluated according to Eq. (3). For this specific sample, the average tortuosity was equal to 1.6.

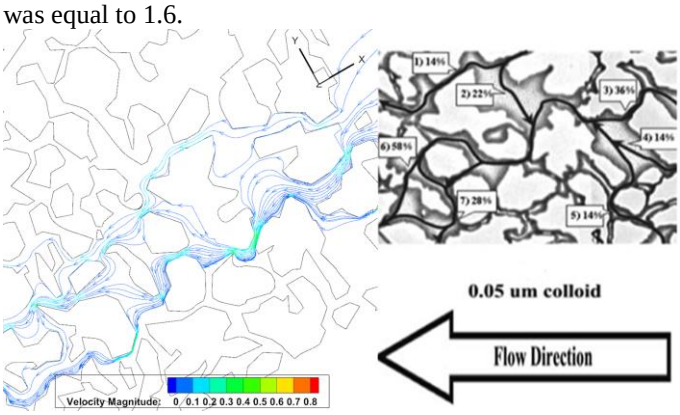

Figure 5: (a) Stream lines distribution with velocity vectors. Higher velocities are calculated at the upper part of the grain (b) Experimental results from Sirivithayapakorn el. al. (21) showing massless particle trajectory (thick black line)

iii. CALCULATION OF PERMEABILITY BASED ON TORTUOCITY

The Darcy law, in its original formulation allows for the calculation of the material permeability based on the macroscopic inlet and outlet parameters (such as pressure drop and mass flow rate). An alternative definition was introduced by Kozeny in 1927 (38) that allows for the calculaiton of permeability based on tortuocity as well as the internal strucutre of the materila such as porocity and average grain diameter. In the following equation

$$k_{per} = \frac{\varepsilon^3}{72(1-\varepsilon)^2\tau^2} d^2 \quad (4)$$

$\boldsymbol{\varepsilon}$ represents the porosity, T tortuosity and d the average grain diameter. The number 72 coresponds to the Kozeny constant (the only value that still has to be tuned) (39).

Based on the above equation and the tortuosity that has been calculated previously as 1.6 we obtain a hydraulic conductivity, k, equal to 6.94616E-05 m/s, which is one order of magnitude larger than the experimental value. The advantage though in comparison to Eq. (1) that provides similar results is that the results are independent of the grid resolution since they depend only to the length of the preferential paths.

a. Multiphase Flow

In the current investigation oil drainage by water injection was the simulation target for the multiphase simulations. The computational domain was initialised with oil (as in the single-phase calculations). Then, water was pumped in and allowed pushing oil out up to the point that all the grid-blocks located in the first 35% of the model were occupied by water. The water-injection simulations are performed at a capillary numbers of the order of 1e-4. Although this capillary number is small (less than 1) implying the important role of the surface tension it is also at a range that viscosity/inertia forces play a role. Figure (6) shows the temporal evolution of water in the pore space at four different snapshots. It is expected that at the capillary number we are currently investigating a transition from a viscous displacement pattern (slow displacement with a balance between capillary forces and viscosity) we move toward a viscous fingering pattern (faster displacement where viscous displacement dominates) will occur. In order this to be captured, an accurate interface reconstruction is needed for the actual velocity of the interphase to be represented. For the presented calculations the use of adaptive mesh was very important for capturing accurately the interface curvature. Here the results correspond to a "fine" grid however coarser grids where tested that resulted in very diffusive interphases. In Fig (7) we show a zoom in of Fig. (6) in order to demonstrate better the interphase reconstruction. Moreover, using this method we were able to capture the thin film of oil between the water and the solid grain that is numerically very challenging to capture.

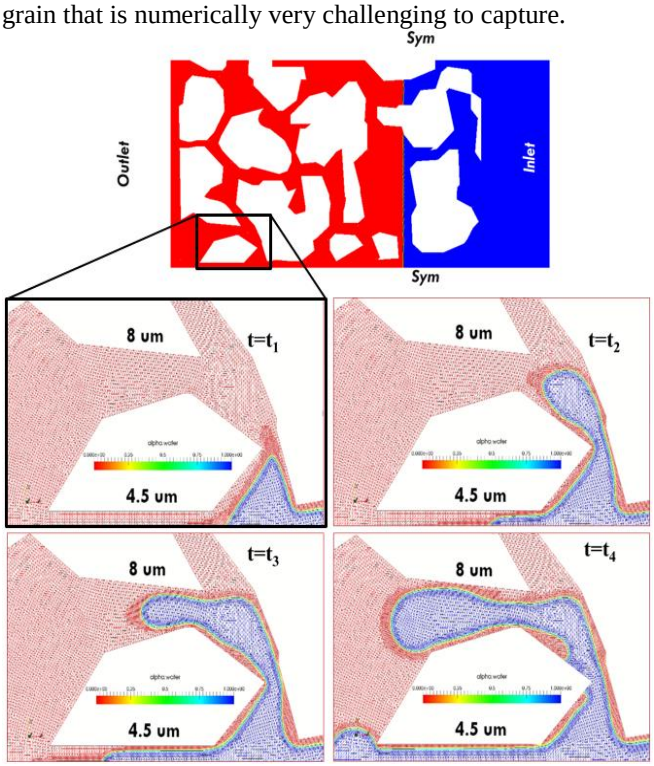

Figure 6: Upper part shows the water initial condition; the four snapshots show the water phase replacing the oil phase after 35% water injection

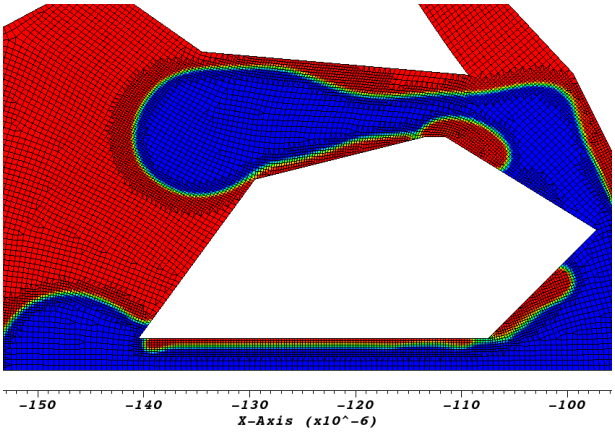

Figure 7: Snapshot for oil film capturing and water snap off using adaptive mesh. Blue represents water volume fraction and red oil.

6. CONCLUSION

Laminar, single- and two-phase flow calculations have been performed inside a pore scale (500 × 500 micron) rock and have allowed estimation of preferential paths of the flow, tortuosity and hydraulic conductivity. A 2D reconstruction of Berea sandstone image was utilised while ANSA® was used for grid construction and refinement. We first tested our numerical tools over various canonical pore arrangements with spherical grains from the literature (not presented here). Then we extended our study to the more realistic geometry of Barea stone that has a complicated internal structure consisting of grains with sharp edges. The results indicate the important role of a good quality grid reconstruction and scale resolution highlighting the need for robust pre and post processing visualization software. More specifically for the case of hydraulic conductivity the results are grid dependent. This grid dependency affects the calculation of rock permeability if a Darcy type formula is used. In order to avoid this deficiency we suggest an alternative method of calculation of permeability based on tortuosity that is much less dependent on the grid. Similar conclusions hold for the multiphase flow cases. Our focus in the multiphase case is capturing fingering effects. It was found that if the grid quality is low then the interphase diffused resulting in the wrong propagation velocity and consequently the transition form viscous displacement to fingering is not captured. We hope that in the future we will be able to examine even larger samples whilst analyzing them at an ever smaller scale. This will bring together the micro and macro levels for the multiphase flow.

7. ACKNOWLEDGMENT

We would like to thank BETA CAE Systems who provided insight and expertise in the use of the pre and post processing tools that greatly assisted the work. We would also like to acknowledge the contribution of The Lloyds Register Foundation. Lloyds Register Foundation helps to protect life and property by supporting engineering-related education, public engagement and the application of research.

8. REFERENCES

1. Raeini AQ, Blunt MJ, Bijeljic B. Modelling two-phase flow in porous media at the pore scale using the volume-of-fluid method. J Comput Phys. 2012 Jul 1;231(17):5653–68.
2. Boccardo G, Marchisio DL, Sethi R. Microscale simulation of particle deposition in porous media. J Colloid Interface Sci. 2014 Mar 1;417:227–37.
3. Gunda NSK, Joseph J, Tamayol A, Akbari M, Mitra SK. Measurement of pressure drop and flow resistance in microchannels with integrated micropillars. Microfluid Nanofluidics. 2013;14(3-4):711–21.
4. Karniadakis G, Beskok A, Aluru N. Microflows and nanoflows: fundamentals and simulation [Internet]. Springer; 2006 [cited 2014 Nov 14]. Available from: http://books.google.co.uk/books?hl=en&lr=&id=vDiLnJHSqvYC&oi=fnd&pg=PA1&dq=G.+E.+Karniadakis+and+A.+Beskok,Microflows:+Fundamentals+and+Simulation%3FSpringer,+New+York,+2001%3F.&ots=R_TlL6F-3k&sig=uAJljZhPrXGpNiVc-Mmlepe8luA
5. Matyka M, Khalili A, Koza Z. Tortuosity-porosity relation in porous media flow. Phys Rev E. 2008;78(2):026306.
6. Christie MA, others. Upscaling for reservoir simulation. J Pet Technol. 1996;48(11):1–004.
7. Gasda SE, Celia MA. Upscaling relative permeabilities in a structured porous medium. Adv Water Resour. 2005 May;28(5):493–506.
8. Szymkiewicz A. Upscaling from Darcy Scale to Field Scale. Modelling Water Flow in Unsaturated Porous Media [Internet]. Springer Berlin Heidelberg; 2013 [cited 2013 Dec 17]. p. 139–75. Available from: http://link.springer.com/chapter/10.1007/978-3-642-23559-7_5
9. Comiti J, Sabiri NE, Montillet A. Experimental characterization of flow regimes in various porous media — III: limit of Darcy's or creeping flow regime for Newtonian and purely viscous non-Newtonian fluids. Chem Eng Sci. 2000 Aug 1;55(15):3057–61.
10. Narsilio GA, Buzzi O, Fityus S, Yun TS, Smith DW. Upscaling of Navier–Stokes equations in porous media: Theoretical, numerical and experimental approach. Comput Geotech. 2009;36(7):1200–6.
11. Larachi F, Hannaoui R, Horgue P, Augier F, Haroun Y, Youssef S, et al. X-ray micro-tomography and pore network modeling of single-phase fixed-bed reactors. Chem Eng J. 2014 Mar 15;240:290–306.
12. Sondergeld C, Ambrose R, Rai C, Moncrieff J. Micro-structural studies of gas shales. SPE Unconventional Gas Conference [Internet]. 2010 [cited 2014 Jan 20]. Available from: http://www.onepetro.org/mslib/servlet/onepetropreview?id=SPE-131771-MS
13. Karpyn ZT, Piri M. Prediction of fluid occupancy in fractures using network modeling and x-ray microtomography. I: Data conditioning and model description. Phys Rev E. 2007 Jul 31;76(1):016315.
14. Spanne P, Thovert J, Jacquin C, Lindquist W, Jones K, Adler P. Synchrotron Computed Microtomography of Porous-Media - Topology and Transports. Phys Rev Lett. 1994 Oct 3;73(14):2001–4.
15. Sahimi M. Characterization of Field-Scale Porous Media: Geostatistical Concepts and Self-Affine Distributions. Flow and Transport in Porous Media and Fractured Rock [Internet]. Wiley-VCH Verlag GmbH & Co. KGaA; 2011 [cited 2014 Jan 6]. p. 109–41. Available from: http://0-onlinelibrary.wiley.com.wam.city.ac.uk/doi/10.1002/9783527636693.ch5/summary
16. Sahimi M. Characterization of the Morphology of Porous Media. Flow and Transport in Porous Media and Fractured Rock [Internet]. Wiley-VCH Verlag GmbH & Co. KGaA; 2011 [cited 2014 Jan 6]. p. 39–108. Available from: http://0-onlinelibrary.wiley.com.wam.city.ac.uk/doi/10.1002/9783527636693.ch4/summary
17. Raoof A, Hassanizadeh SM. A new method for generating pore-network models of porous media. Transp Porous Media. 2010;81(3):391–407.
18. Ovaysi S, Piri M. Direct pore-level modeling of incompressible fluid flow in porous media. J Comput Phys. 2010;229(19):7456–76.
19. BETA CAE Systems S.A. - ANSA pre-processor [Internet]. [cited 2015 Jun 8]. Available from: http://www.beta-cae.gr/ansa.htm
20. Hornbrook JW, Castanier LM, Pettit PA, others. Observation of foam/oil interactions in a new high-resolution micromodel. SPE Annual Technical Conference and Exhibition [Internet]. Society of Petroleum Engineers; 1991 [cited 2015 Jun 3]. Available from: https://www.onepetro.org/conference-paper/SPE-22631-MS
21. Sirivithayapakorn S, Keller A. Transport of colloids in saturated porous media: A pore-scale observation of the size exclusion effect and colloid acceleration. Water Resour Res. 2003;39(4):1109.
22. Øren P al-E, Bakke S. Reconstruction of Berea sandstone and pore-scale modelling of wettability effects. J Pet Sci Eng. 2003;39(3):177–99.
23. Øren P al-E, Bakke S. Process based reconstruction of sandstones and prediction of transport properties. Transp Porous Media. 2002;46(2-3):311–43.
24. Keller AA, Blunt MJ, Roberts APV. Micromodel Observation of the Role of Oil Layers in Three-Phase Flow. Transp Porous Media. 1997 Mar 1;26(3):277–97.
25. Whitaker R, Breen D, Museth K, Soni N. Segmentation of biological volume datasets using a level-set framework. Volume Graphics 2001 [Internet]. Springer; 2001 [cited 2015 Jun 8]. p. 249–63. Available from: http://link.springer.com/chapter/10.1007/978-3-7091-6756-4_17
26. Fourie W, Said R, Young P, Barnes DL. The simulation of pore scale fluid flow with real world geometries obtained from X-ray computed tomography. Proceedings of the Boston COMSOL Conference

[Internet]. 2007 [cited 2015 Jun 8]. Available from: https://www.comsol.it/paper/download/15042/Fourie.pdf

27. Rigby SP, Fletcher RS, Raistrick JH, Riley SN. Characterisation of porous solids using a synergistic combination of nitrogen sorption, mercury porosimetry, electron microscopy and micro-focus X-ray imaging techniques. Phys Chem Chem Phys. 2002;4(14):3467–81.
28. Liu J, Regenauer-Lieb K. Application of percolation theory to microtomography of structured media: Percolation threshold, critical exponents, and upscaling. Phys Rev E. 2011;83(1):016106.
29. Xiao Z, Yang D, Yuan Y, Yang B, Liu X. Fractal pore network simulation on the drying of porous media. Dry Technol. 2008;26(6):651–65.
30. Zhou Y. Pore scale modeling of capillary pressure curves in 2D rock images. 2013 [cited 2013 Dec 23]; Available from: http://brage.bibsys.no/uis/handle/URN:NBN:no-bibsys_brage_46963
31. OpenFOAM® - The Open Source Computational Fluid Dynamics (CFD) Toolbox [Internet]. [cited 2015 Jun 8]. Available from: http://www.openfoam.com
32. Georgoulas A, Koukouvinis P, Gavaises M, Marengo M. Numerical investigation of quasi-static bubble growth and detachment from submerged orifices in isothermal liquid pools: The effect of varying fluid properties and gravity levels. Int J Multiph Flow. 2015;74:59–78.
33. How Does Water Injection Work? [Internet]. [cited 2015 Jun 8]. Available from: http://www.rigzone.com/training/insight.asp?insight_id=341&c_id=4
34. Standard A. D2434-68 (2006) Standard Test Method for Permeability of Granular Soils (Constant Head). ASTM International, West Conshohocken, PA, DOI: 10.1520/D2434-68R06.
35. Bear J. Dynamics of fluids in porous media [Internet]. Courier Dover Publications; 1988 [cited 2014 Jun 19]. Available from: http://books.google.co.uk/books?hl=en&lr=&id=fBMeVSZ_3u8C&oi=fnd&pg=PP1&dq=dynamics+of+fluids+in+porous+media&ots=mfayulXMEz&sig=ut67gcnlbHC6NZSL8XzOLDifo38
36. Fair GM, Hatch LP, Hudson HE. Fundamental factors governing the streamline flow of water through sand [with discussion]. J Am Water Works Assoc. 1933;1551–65.
37. Bear J, Tsang CF, De Marsily G. Modeling flow and contaminant transport in fractured rocks. Flow Contam Transp Fract Rock. 1993;1–37.
38. Chapuis RP, Aubertin M. On the use of the Kozeny-Carman equation to predict the hydraulic conductivity of soils. Can Geotech J. 2003 Jun;40(3):616–28.
39. Nojabaei B, Johns RT, Chu L, others. Effect of capillary pressure on phase behavior in tight rocks and shales. SPE Reserv Eval Eng. 2013;16(03):281–9.